



Monitoring aerosol optical depth during the Arctic night: Instrument development and first results

Mauro Mazzola^{a,*}, Robert S. Stone^b, Natalia Kouremeti^c, Vito Vitale^a, Julian Gröbner^c, Kerstin Stebel^d, Georg H. Hansen^d, Thomas C. Stone^e, Christoph Ritter^f, Simone Pulimeno^{a,g}

^a National Research Council, Institute of Polar Sciences, Via P. Gobetti 101, Bologna 40129, Italy

^b National Oceanic and Atmospheric Administration, 325 Broadway, Boulder 80305, CO, USA

^c Physikalisch-Meteorologisches Observatorium Davos, Dorfstrasse 33, Davos 7260, Switzerland

^d Norwegian Institute for Air Research, Instituttveien 18, Kjeller 2007, Norway

^e U.S. Geological Survey, 2255 Gemini Rd, Flagstaff 86001, AZ, USA

^f Alfred Wegener Institute for Polar and Marine Research, Telegrafenberg, Potsdam 14473, Germany

^g Ca' Foscari University of Venice, Department of Environmental Sciences, Informatics and Statistics, Via Torino 155, Venice, 30172, Italy

ARTICLE INFO

Keywords:

Aerosol
AOD
Photometry
Arctic
Polar night
Moon

ABSTRACT

Moon-photometric measurements were made at two locations in the Arctic during winter nights using two different modified Sun photometers; a Carter Scott SP02 and a Precision Filter Radiometer (PFR) developed at PMOD/WRC. Values of aerosol optical depth (AOD) were derived from spectral irradiance measurements made at four wavelengths for each of the devices. The SP02 was located near Barrow, Alaska and recorded data from November 2012 to March 2013, spanning five lunar cycles, while the PFR was deployed to Ny-Ålesund, Svalbard each winter from February 2014 to February 2019 for a total of 56 measurement periods. A methodology was developed to process the raw data, involving calibration of the instruments and normalizing measured spectral irradiance values in accordance with site-specific determinations of the extraterrestrial atmospheric irradiance (ETI) as Moon phase cycled. Uncertainties of the derived AOD values were also evaluated and found to be in the range, 0.006–0.030, depending on wavelength and which device was evaluated.

The magnitudes of AOD determined for the two sites were in general agreement with those reported in the literature for sunlit periods just before and after the dark periods of Arctic night. Those for the PFR were also compared with data obtained using star photometers and a Cimel CE318-T, recently deployed to Ny-Ålesund, showing that Moon photometry is viable as a means to monitor AOD during the Arctic night. Such data are valuable for more complete assessments of the role aerosols play in modulating climate, the validation of AOD derived using various remote sensing techniques, and applications related to climate modeling.

1. Introduction

Atmospheric aerosols play an important role in shaping planetary climate. Their interaction with solar and terrestrial radiation, involving both scattering and absorption, alters the Earth-atmosphere energy balance in complicated ways making it difficult to quantify their effects. Further, aerosols modify cloud properties, such as particle droplet size and liquid water content. The influence of aerosols on a global scale is still fraught with great uncertainty (IPCC, 2023); and particular to this study, the dearth of data during long periods of darkness during Polar winter needs to be addressed. One goal of the Polar-AOD program (Tomasi et al., 2012; Mazzola et al., 2012) is to establish a network of

stations across both the Arctic and Antarctic to address this need. AOD (aerosol optical depth) at a given wavelength is a measure of the total attenuation of solar irradiance reaching the earth's surface (at that specific wavelength) by aerosols suspended in the atmosphere. It is a columnar integration of the particulates of many types, sometimes referred as turbidity. Measuring AOD over a range of wavelengths is common and permits evaluation of relative particle size.

The monitoring of aerosol content in the vertical column is currently conducted using both ground-based and space-borne platforms. Passive techniques utilize the extinction and/or scattering of solar radiation to retrieve this quantity through the inversion of measured signals (Shaw, 1983; Kaufman and Joseph, 1982). LIDARs use a laser beam as a light

* Corresponding author.

E-mail address: mauro.mazzola@cnr.it (M. Mazzola).

source so can operate at night. They exhibit superior performance during the night because the absence of solar radiation reduces the spurious light entering the detector (Hoffmann et al., 2010). Hence, techniques for aerosol monitoring during the night already exist, including star photometry, where the sources of radiation are the stars, like the Sun, emitting a constant stream of light (Pérez-Ramírez et al., 2008).

There are compelling reasons to quantify aerosol columnar content during the night. These include studying the effects of aerosols on long-wave radiation, both direct and as they interact with clouds (Lubin and Vogelmann, 2006), complementing other measurements such as backscatter profiles obtained by LIDARs (both ground and satellite-based, see Brunamonti et al. (2021)), detecting transport of aerosols from lower latitudes to polar regions during winter (Zhao et al., 2022) and, importantly, filling gaps in AOD climatologies from which more complete evaluations of the changing climate can be made (Stone et al., 2014b).

One of the earliest attempts to utilize the Moon as a source of radiation for photometric measurements was undertaken by (Esposito et al., 1998). They captured Moon-reflected radiation in the spectral range of 320–640 nm using a system consisting of a scanning monochromator, a focal lens, and a photomultiplier. Applying the Langley plot method to a night of measurements near Potenza, in the South of Italy, the authors derived calibration factors and AOD simultaneously. The same technique was employed for a four-day period in a desert site in Namibia (Esposito et al., 2003).

Herber et al. (2002) reported, for the first time, continuous day and night AOD measurements in the Arctic using Sun, Moon, and star photometry across different periods of the year. In terms of lunar measurements, they employed the same technique as Esposito et al. (1998), constructing a Langley plot for each suitable measurement period and applying it to that specific period. This approach helped overcoming challenges related to variations in lunar brightness arising from the Moon's ever-changing phase.

Berkoff et al. (2011) introduced the approach adopted in the present study, utilizing an empirical model to replicate the lunar *exo*-atmospheric irradiance (EAI) specific to each time step and location as well as wavelength. They employed the highest gain setting of an unmodified Cimel CE318 sun-photometer for measurements and evaluated the existing capabilities, while identifying enhancements required for day/night operation.

Barreto et al. (2013a) presented a new lunar photometer prototype, the Cimel CE318-U. This prototype featured a built-in lunar tracking system and an improved signal amplification system for channels ranging from 440 to 1640 nm. Additionally, the study introduced three methods for calibrating the new lunar photometer. The same instrument was employed by Barreto et al. (2013b) for the retrieval of precipitable water vapor during the night. An advanced version of this instrument, the CE318-T, was introduced in Barreto et al. (2016). The CE318-T demonstrated the capability of making both daytime and nighttime photometric measurements using the Sun and the Moon as light sources (Perrone et al., 2022; Herrero del Barrio et al., 2023). The AEROSOL RObotic NETwork (AERONET) is adopting this instrument as the standard for its network (https://aeronet.gsfc.nasa.gov/cgi-bin/webtool_aod_v3_lunar, accessed 01/05/2024).

Recently a modified POM-02 from Prede has been used by Uchiyama et al. (2019) for estimating nocturnal AOD near Tokyo (Japan), showing similar reliability between day and nighttime measurements. Attempts of retrieving nighttime AOD from satellite observations of reflected moonlight have also been made over the U.S., by Zhou et al. (2021) but obtaining less accurate when compared with AERONET or Cloud-Aerosol Lidar with Orthogonal Polarisation (CALIOP) data.

In this paper we report the results from lunar measurements at two sites in the Arctic region, Barrow (Alaska) and Ny-Ålesund (Svalbard), using two different instruments. In Section 2 we illustrate the methodology, including calibration and uncertainties assessment, and the adopted instrumentation, in Section 3, we show the results of the

measurements. Finally, in Section 4 we draw conclusion about this emerging technology.

2. Methodology and instrumentation

2.1. Differences between Moon and Sun photometry

There are two primary differences between Sun and Moon photometry: (i) the very large variation in the reflected irradiance from the Moon during a full lunar cycle; this is attributed mainly to its ever changing phase but also its distance from the Earth, and (ii) the extremely low magnitude of the reflected sunlight Earth's surface relative to the solar constant value.

Sun photometry involves the application the Lambert-Beer law (Shaw et al., 1973)

$$J_{\lambda} = \frac{J_{0,\lambda}}{R^2} e^{-m\tau_{\lambda}} \quad (1)$$

where the signal measured at the point of observation at wavelength λ is denoted as J_{λ} , with $J_{0,\lambda}$ representing the calibration factor at the same wavelength, i.e., the signal measured hypothetically at the top of the atmosphere (TOA) at the mean Earth-Sun distance r_0 . Here, R is the ratio between the actual Earth-Sun distance r and r_0 , hence numerically equivalent to the Sun-Earth distance expressed in astronomical units (AU), m denotes the relative optical air mass, and τ_{λ} represents the atmospheric total optical depth. Total optical depth is the sum of contributions from Rayleigh scattering by air molecules, absorption due to minor gases, primarily ozone and nitrogen dioxide, and extinction along the path due to aerosols.

When utilizing the Moon as a light source (or target), it is essential to acknowledge that its brightness, unlike the Sun, is not constant. The brightness of the Moon as observed from Earth varies based on the actual geometric configuration between the Sun, the Moon, and the observer, encompassing factors such as the lunar phase and libration (Uchiyama et al., 2019). Librations occur due to the Moon having an elliptical orbit around the Earth and because its axis is not aligned with its elliptical plane and wobbles slightly; thus exposing different regions over time as observed from the Earth. The amount of reflected sunlight reaching the top of the atmosphere is proportional to the Moon albedo, and also the Moon-observer distance needs to be considered:

$$J_{\lambda} = \frac{J_{0,\lambda}^*}{(Rd)^2} e^{-m\tau_{\lambda}} \quad (2)$$

with

$$J_{0,\lambda}^* \propto \frac{A_{\lambda} \Omega E_{\lambda}}{\pi} \quad (3)$$

where d is the ratio between the actual Moon-observer distance and the mean radius of the Moon's orbit around the Earth (384,400 km), A_{λ} represents the disk-equivalent lunar albedo at the wavelength λ , Ω denotes the solid angle of the Moon, and E_{λ} is the standard extraterrestrial solar irradiance at the wavelength λ (Ω and E_{λ} both evaluated at standard distances, see Kieffer and Stone (2005)). In brief, the right part of the equation describes the lunar-reflected irradiance at the wavelength λ .

The USGS lunar calibration program has developed the RObotic Lunar Observatory (ROLO), a model of the equivalent reflectance of the lunar disk as a function of geometry, using an empirically derived analytic form based on the primary geometric variables, i.e. absolute phase angle, selenographic latitude and longitude of the observer, and selenographic longitude of the Sun (Kieffer and Stone, 2005). The validity of this model extends to the first and third quarters of the Moon phase, encompassing lunar albedo and the Moon-observer distance, both of which exhibit continuous variations throughout the lunar cycle.

By normalizing the measured signals with respect to the reflected

irradiance, the resulting formula mirrors that used in sun photometry

$$J_{\lambda}^* = \frac{J_{0,\lambda}^*}{(Rd)^2} e^{-m\tau_{\lambda}} \quad (4)$$

with

$$J_{\lambda}^* = \frac{J_{\lambda}}{\left(\frac{A_{\lambda} \Omega E_{\lambda}}{\pi}\right)} \quad (5)$$

Notably, the new signals and calibration constants remain independent of the specific lunar phase. It is worth noting here that the absolute value of the irradiance is not needed here, as the Langley method brings to a relative calibration of the instrument. For this work, the EAI values were provided by the ROLO developers at USGS for the spectral channels of the adopted instruments. A freely accessible implementation of the original algorithm named RIMO (ROLO Implementation for Moon-photometry Observation) has been released (Barreto et al., 2017, 2019; Román et al., 2020).

The radiation signals reflected by the Moon and reaching the Earth have been estimated to be between 5 and 6 orders of magnitude smaller than those directly emitted by the Sun. This discrepancy varies depending on the wavelength and falls within the spectral range typically utilized for aerosol measurements (300–1000 nm). Traditional sun photometers are, therefore, incapable of measuring these extremely low signals. As a result, specific modifications are necessary to adapt them for this purpose.

Details on the procedure to obtain AOD from τ_{λ} using Eq. 1 can be found in Mazzola et al. (2010). From the AOD spectral values it is then possible to calculate the Angström Exponent α (Ångström, 1929), a parameter that describes how AOD depends on wavelength and that is inversely related to the average size of the particles (Schuster et al., 2006). In this study, a $\log - \log$ fit between AOD and λ was used to evaluate α .

2.2. Instrumentation

In this study we used two different modified Sun photometers at two sites: a Carter Scott (now Middleton Solar Inc.) SP02 (Forgan, 2005) that has been modified at the NOAA/GMD laboratories in Boulder, CO, in order to increase the amplification, and a Precision Filter Radiometer (PFR) (Wehrli, 2005) designed by PMOD/WRC and modified for the same aim.

The primary modification of the SP02 involved amplifying its signal response to enable measurements of very low light intensity of lunar reflected light. Tests were made systematically to achieve the best signal to noise (S/N) ratio at each of four wavelengths; 425, 500, 675 and 862 nm. The device was mounted on an Eppley SMT solar tracker that was reprogrammed to track the Moon. The tracker was specially lubricated to assure operation at temperatures as cold as -50°C . The SP02 was encapsulated with heat tape and then insulated. The device was thermally controlled to a set-point of 15°C , using a PID (proportional-integral-derivative) controller to assure electronic stability, both during calibration and when operating in the field. Thermal control was considered to be a very important design feature to assure the acquisition of consistent, high-quality data. Data were collected once per minute by averaging 12 one-second values of voltage before and after each time step, and recorded by a Campbell Scientific CR10X datalogger. The system included a webcam fitted to the tracker to collect images of the Moon each half hour during observing cycles. Webcam images were useful for identifying contamination by thin clouds during data analysis. Once tested at NOAA Boulder, CO laboratory, the system was shipped to the NOAA Mauna Loa Observatory (MLO) for calibrations during summer 2012, and finally to Barrow to be operated through the 2012–2013 winter. The development of the NOAA proto-type lunar SP02 and its deployment to Barrow during winter 2012/2013 is further

Table 1

Wavelengths of the 4 channels for the SP02 and PFR (both versions) photometers.

	Ch1	Ch2	Ch3	Ch4
SP02	425 nm	500 nm	675 nm	862 nm
PFR/PFR2015	412 nm	500 nm	675 nm	862 nm

described in Stone et al. (2014a).

Regarding the PFR, modifications were implemented by increasing the first and second stage amplifications, resulting in a supplementary gain of up to 10^4 . Additionally, the filter apertures' diameter was enlarged from 3 to 6 mm, contributing to another $4\times$ gain. To address the challenges posed by weak signals at shorter wavelengths, the original 368 nm filter in the PFR was replaced with one at 675 nm. The other wavelengths are centered at 412, 500 and 862 nm. This instrument conducts measurements at the top of each minute and is equipped with a shutter system that enables the measurement of dark signals between consecutive measurements. In 2015, further enhancements were made to improve the signal-to-noise ratio. Notably, the Campbell CR10X datalogger typically used with the PFR system was replaced with a SACRAM OWEL datalogger. After that, the instrument has been fully characterized using the radiometric calibration laboratory facilities of PMOD/WRC. This included filter function, sensors response linearity and absolute irradiance calibration. From here on we will refer to this second version as PFR2015, to distinguish it from the first modified PFR when not implicitly obvious.

Table 1 reports the central wavelengths of the 4 channels for each instrument. In the following, explicit wavelengths or labels of the form ChN (with N assuming values between 1 and 4) will be used indifferently depending on the context.

Fig. 1 shows the raw signals (upper panel) and normalized (4 signals (lower panel) obtained using the modified PFR for two measurement periods: one during the first quarter, with a 50 % illuminated fraction (left part), and another near the full Moon with a 90 % illumination fraction (right part). As observed in the upper panel, transitioning from the first quarter to near full Moon conditions results in raw signals increasing by approximately a factor of 5. Only a small portion of this increase can be attributed to the change in Moon elevation, which shifts from 24.7° to 26.1° between the first and second period. In contrast, the signal noise remains similar in both cases, resulting in a higher signal-to-noise (S/N) ratio for the near full Moon scenario (appreciable only for the 675 nm channel in the figure). It's important to note that the peak of the measured signals does not align with the maximum elevation in time, owing to the complex geometry of the system.

After normalization the signals become comparable in strength for the two periods, making it easier to appreciate the lower S/N ratio in the case of 50 % Moon illumination. Simultaneously, it is possible to observe the shift of the signals' maxima towards the position of the elevation maxima.

2.3. Calibration

As anticipated, the instrument calibration was conducted using the Langley plot method. This method involves extrapolating the logarithm of normalized signals as a function of air mass towards the zero value (Barreto et al., 2013a). Typically, this method yields better results in stable atmospheric conditions with respect to particle content. Consequently, it is commonly employed at high-altitude mountain sites where aerosol extinction and atmospheric pressure changes occurring over a few hours are generally minimal.

The SP02 photometer was calibrated at the Mauna Loa Observatory (MLO, $19^{\circ} 32' \text{N}$, $155^{\circ} 34' \text{W}$, 3397 m a.s.l.) over four lunar cycles between August and October 2012. The results obtained were applied to data collected then adopted for subsequently during winter 2012/2013 at Barrow. In contrast, the PFR instruments underwent its initial

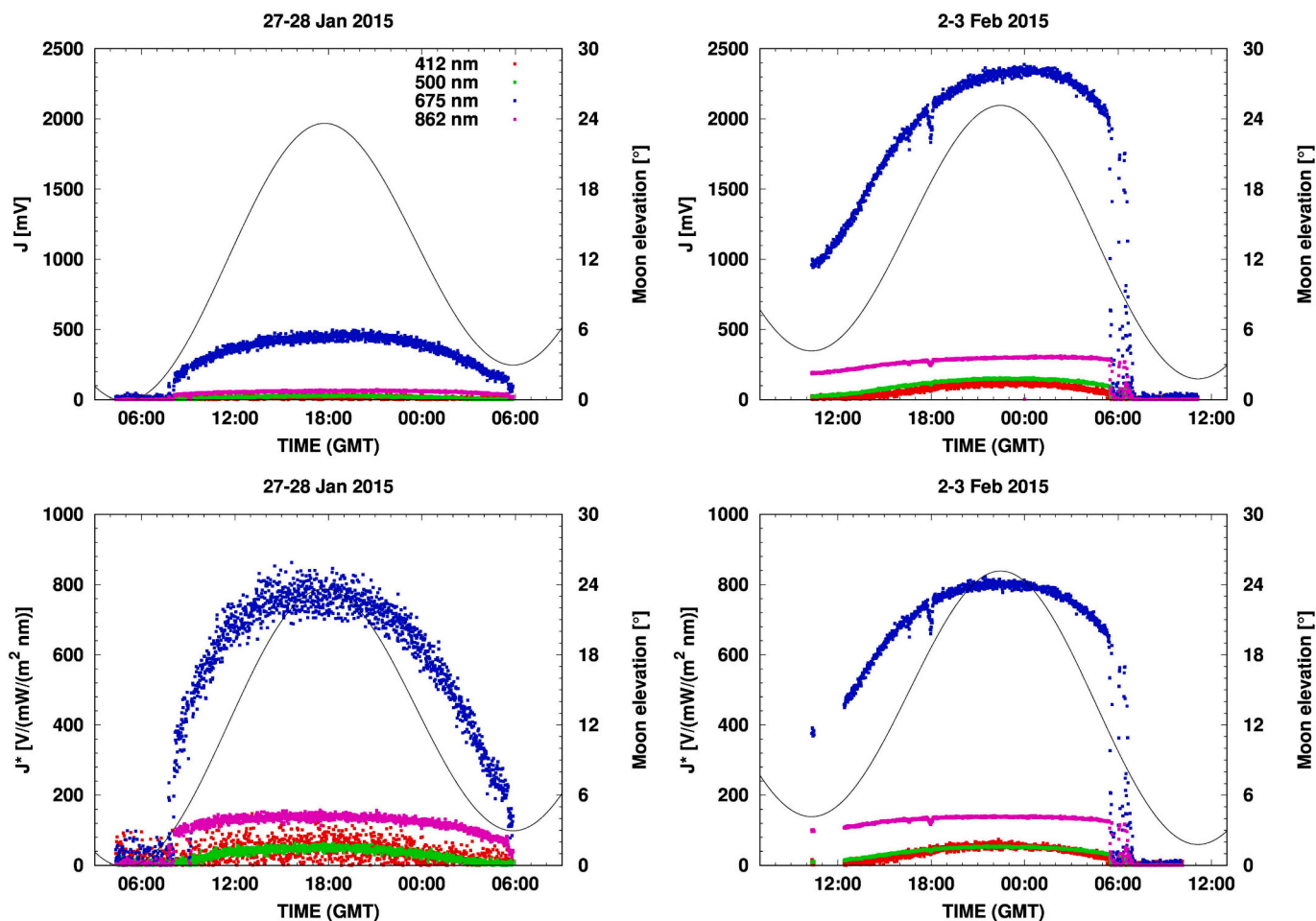


Fig. 1. Raw signals (upper panel) and normalized signals (lower panel) for the four channels of the Moon PFR (first version) obtained at Ny-Ålesund for two measurement periods: one at the first quarter with 50 % of illuminated fraction (left part) and another near the full Moon with 90 % of illuminated fraction (right part). The Moon's elevation is also shown in each panel by the black line.

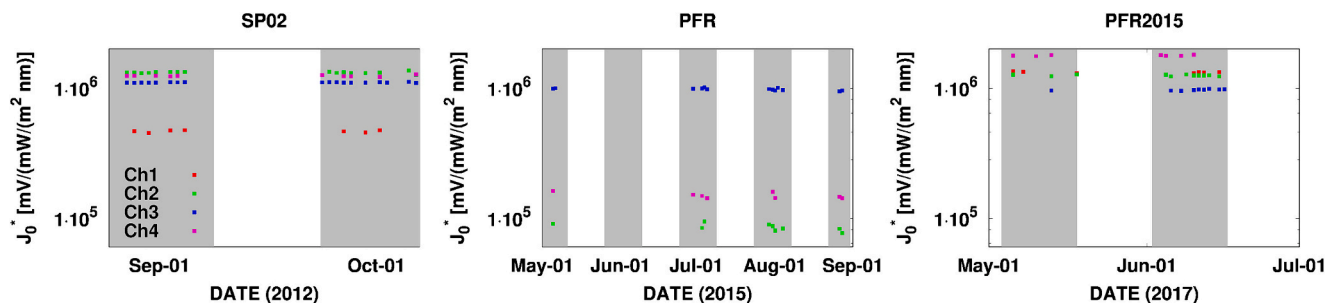


Fig. 2. Time evolution of the calibration factors obtained using the Langley method for the SP02 photometer at Mauna Loa (first panel on the left) and for the PFR photometers at Izaña (PFR in the panel in the middle and PFR2015 in the panel on the right). Shaded areas indicate the first-third quarter moon phase periods.

calibration at the Izaña Atmospheric Observatory (IZO, 28° 18' N, 16° 29' W, 2373 m a.s.l.) over four lunar cycles during the summer of 2015 (May–September), and these results were subsequently applied to measurements previously recorded at Ny-Ålesund. After the modifications applied to the instrument during 2015, the instrument was calibrated in 2017 at the same site during the inter-comparison campaign whose results are described in Barreto et al. (2019).

The accuracy of a valid Langley plot was evaluated by both an automated method, as described in Mazzola et al. (2010), but also by visual inspection. Due to the lower S/N ratio values of lunar observations compared to solar measurements, the root mean square difference (RMSD) limit for the fits was set to 0.020 for SP02 and the first version of

lunar PFR instead of the 0.006 value suggested by Harrison and Michalsky (1994) for the Sun. For the calibration of the PFR2015 we used the original value of Harrison and Michalsky (1994) for this parameter. The values of RMSD will be used to evaluate the contribution of measured signals to AOD uncertainties (see Section 2.4). Fig. 2 shows the time series of the calibration factors obtained for the two instruments.

Table 2 presents the calibration constants as average values for the two instruments, along with associated standard deviations and the number of valid fits N . The RMSD average value for each set of Langley results is also reported ($< \sigma_y >$). For the PFR, the factors obtained both

Table 2

Calibration factors statistics for the four spectral channels of both the SP02 and PFR photometers. $\langle \sigma_y \rangle$ is the RMSD average value for each set of Langley results. As reported in Table 1, the wavelength of the first channel is 425 nm for SP02 and 412 nm for PFR and PFR2015.

		425/412 nm	500 nm	675 nm	862 nm
SP02	Average	465.1e+3	131.6e+4	110.3e+4	124.0e+4
	St.Dev.	8.7e+3	2.0e+4	5.8e+4	1.4e+4
		(1.9 %)	(1.5 %)	(0.5 %)	(1.2 %)
	N	7	16	18	10
	$\langle \sigma_y \rangle$	0.019	0.005	0.003	0.003
PFR	Average	–	83.5e+3	97.9e+4	145.3e+3
	St.Dev.	–	2.5e+3	2.0e+4	3.7e+3
		–	(2.9 %)	(2.1 %)	(2.6 %)
	N	–	5	13	6
	$\langle \sigma_y \rangle$	–	0.014	0.007	0.014
PFR2015	Average	132.0e+4	125.0e+4	96.7e+4	178.0e+4
	St.Dev.	1.6e+4	1.7e+4	1.2e+4	1.5e+4
		(1.2 %)	(1.4 %)	(1.2 %)	(0.8 %)
	N	7	11	9	7
	$\langle \sigma_y \rangle$	0.004	0.003	0.002	0.002

before and after the modifications of 2015 are reported.

As can be seen from Fig. 2 and Table 2 no valid values were obtained for the channel at 412 nm of PFR, due to the adopted RMSD threshold value. Consequently, no AOD values were obtained for this instrument and this channel (see e.g. Fig. 4).

Additionally, Langley plot analyses were performed using operational data at the respective observatories; in all cases yielding similar values. Field calibrations were very reassuring that derived AOD values were of high quality over the entire period of observation.

2.4. Error analysis

The Lambert-Beer law implies that the uncertainty in AOD can be represented as the quadratic sum of terms arising from the various parameters involved in the equation (refer to, for example, Mazzola et al. (2010), Eq. 5).

In Sun photometry, the term associated with errors in the signal measurement is usually neglected, being much smaller than the other terms. This is not the case when measuring very low irradiance reflected from the Moon as is evident looking at Fig. 1. This term should take into account also the uncertainty due to signal normalization itself (Eq. 4), i. e. that associated with the EAI calculation. In that sense it would read as the quadratic sum of the term associated with the raw signals and that associated with the normalization

$$\left(\frac{\Delta J_{\lambda}^*}{J_{\lambda}^*}\right)^2 + \left(\frac{\Delta k_{\lambda}}{k_{\lambda}}\right)^2 \quad (6)$$

where k_{λ} is the term on the right side of Eq. 2. The uncertainty on k_{λ} has been estimated by the ROLO developers to be 3 % in the 300–1000 nm spectral range (personal communication). Given the challenging nature of signal evaluation, we opted to estimate the uncertainty associated with the normalized signals. This estimation was accomplished by leveraging measurements obtained under clear sky conditions.

The uncertainty of the normalized signals has been evaluated by considering their ripple around the Langley fit line for the periods selected as good for calibration. In that sense, the $\langle \sigma_y \rangle$ values reported in Table 2 are the averages of the RMSD of the logarithm of the normalized signals in the Langley fits. As $d(\log(x)) = dx/x$, the term $\Delta J_{\lambda}^*/J_{\lambda}^*$ can be taken equal to $\langle \sigma_y \rangle$. Its values ranged between 0.3 % and 1.9 % for the SP02 and between 0.7 % and 1.4 % (first version) and 0.2 % and 0.4 % (second version) for the PFR.

The uncertainty associated with the calibration constant was assessed using the relative standard deviation linked to its average value. As indicated in Table 2, it was observed to vary across different

Table 3

Uncertainties associated with the normalized signals and calibration coefficients, as well as total uncertainties obtained considering also Rayleigh and absorption contribution to AOD at the considered wavelengths.

		Channel	$\Delta J^*/J^*$	$\Delta J_{0}^*/J_{0}^*$	$\Delta \tau$
SP02		425 nm	0.019	0.019	0.027
		500 nm	0.005	0.015	0.016
		675 nm	0.003	0.005	0.006
		862 nm	0.003	0.012	0.012
PFR		412 nm	–	–	–
		500 nm	0.014	0.044	0.046
		675 nm	0.007	0.021	0.022
PFR2015		862 nm	0.014	0.026	0.030
		412 nm	0.004	0.029	0.030
		500 nm	0.003	0.018	0.018
		675 nm	0.002	0.022	0.022
		862 nm	0.002	0.022	0.022

channels, ranging between 0.5 % and 1.9 % for SP02, between 2.1 % and 4.4 % for PFR and between 1.8 %–2.9 % for the PFR2015.

Uncertainties associated with Rayleigh scattering and gas absorption were derived from Mazzola et al. (2010), noting that the MultiFilter Rotating Shadowband Radiometer (MFRSR) instrument shares similar spectral channels as the SP02 and PFR, and having adopted identical algorithms for these minor corrections.

Table 3 lists for each wavelength the uncertainties evaluated for the normalized signals and calibration coefficients, as well as the total values obtained by summing the quadrature terms, including Rayleigh and gas absorption as stated above. In practice, the first two terms depend on the value of the optical air mass. In the table values are reported only for $m = 1$. Due to the inclination of the lunar orbital plane with respect to the Earth ecliptic (5°), in the polar circle the Moon reaches a maximum daily elevation of about 52° , that turns in m values always greater than 1.6. Conversely, there are days in which the Moon doesn't rise at all. It is worth noting here that the contributions from Rayleigh and gas absorption are negligible in comparison to the total uncertainties. Overall, these uncertainties vary between 0.006 and 0.027 for SP02, between 0.022 and 0.046 for the PFR and between 0.018 and 0.030 for the PFR2015.

It is worth noting here that, for AOD values as low as those usually found in remote areas as the Arctic, such uncertainties values on AOD brings to very high uncertainties values on α (e.g. 30 % or 0.5 in absolute values, see for example Toledano et al. (2007) or Mazzola et al. (2012)).

3. Measurements and results

3.1. Barrow, Alaska

Data from five lunar cycles were acquired at the Barrow Atmospheric Baseline Observatory ($71^\circ 19' N$, $156^\circ 37' W$, 11 m a.s.l.), about 8 km northeast of the village of Utqiagvik (Alaska), from the end of November 2012 through March 2013. As described above, the photometer was installed on a re-programmed solar tracker in order to track the Moon. It was paired with a webcam in order to capture lunar images useful to visually check both the tracking and to identify the presence of clouds if contamination was suspected during processing. Fig. 3 shows the AOD obtained from two different days of measurement, one for low Moon illumination (59 %, near the first quarter) and one for high illumination (92 %, near full Moon).

As expected, the AOD values are noisier at low illumination as a consequence of the lower S/N ratios. Also, AODs at different wavelengths show different levels of noise (evaluated here as average of the standard deviations associated to hourly means) associated with the different characteristics of the filters, of the sensors and of the electronic of amplification: about 56 % at 412 nm, 13 % at 500 nm, 39 % at 675 nm and 31 % at 865 nm near the first quarter and 34 %, 4 %, 14 % and 6 % near full Moon for the same wavelengths. The same behavior is shown

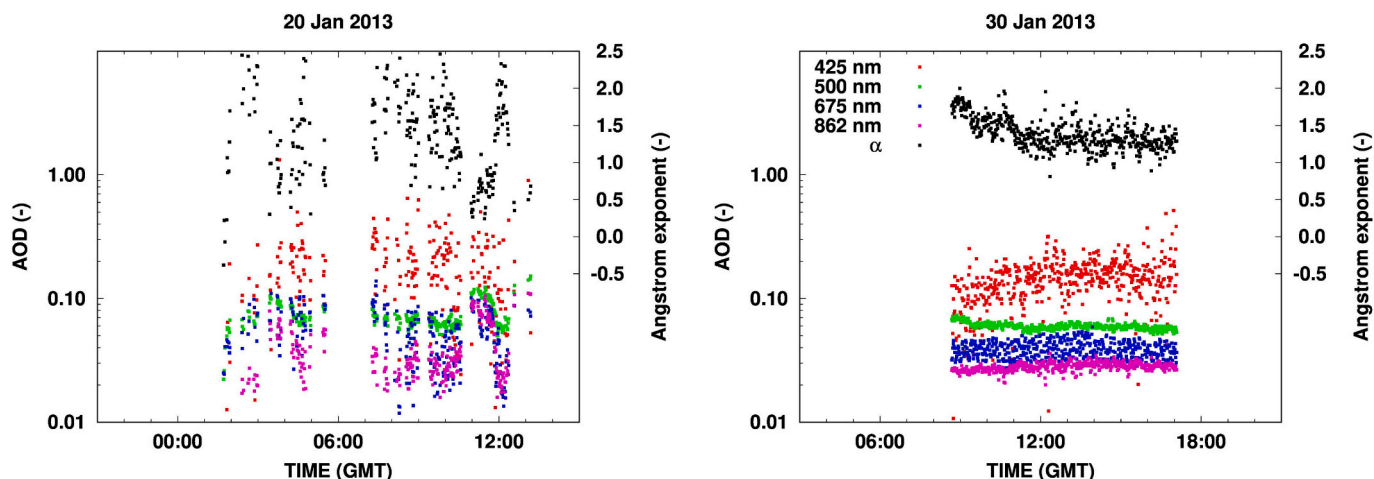


Fig. 3. Spectral AOD obtained using the SP02 at Barrow on January 20, 2013, with 59 % of lunar illumination (left), and on January 30, 2013, with 92 % illumination (right).

Table 4

Number of lunar cycles per winter season and total number of measurement periods for Ny-Ålesund.

Season	Lunar cycles	Measurement periods
2013/2014	1 (Feb)	2
2014/2015	4 (Oct-Feb)	15
2016/2017	1 (Jan)	4
2017/2018	5 (Nov-Mar)	13
2018/2019	5 (Oct-Feb)	22

for the Angström Exponent α (Ångström, 1929) (28 % and 10 % at low and high illumination, respectively).

Fig. B.7 displays hourly values of AOD at 500 nm and α , along with their respective standard deviations, across all available measurement periods. The majority of AOD values fell within the range of 0.05 to 0.10, while the α values ranged between 1 and 2, predominantly centered around 1.5.

The recorded AOD values for both parameters aligned well with the minimum values reported by Tomasi et al. (2012) for the non Arctic Haze periods, when measurements were made during sunlit periods. This may indicate that particle transport had not yet begun during the period examined (December and January).

On November 26, 2012 around noon, a rapid increase in AOD (from 0.05 to 0.20) and a concurrent decrease in α (from 1.5 down to less than

0.5) was detected. This was due to the presence of thin cirrus cloud as evidenced by images taken by the webcam (not shown). A similar event occurred the morning of January 20, 2013. In contrast, very high values of α (~ 2) were measured on December 28, 2012, probably associated with the presence of much smaller aerosol particles. This inverse relationship between unexpectedly high values of AOD when the α is very low (or negative) is often used to constrain determinations of AOD when developing climatologies; i.e., to omit contamination by thin clouds (Stone et al., 2014b).

3.2. Ny-Ålesund, Svalbard

At Ny-Ålesund the instrument was installed at the Sverdrup Observatory (78° 55' N, 11° 55' E, 16 m a.s.l.) on a 2AP Kipp & Zonen solar tracker driven by a Python code based on the lunar position calculator by Darin Koblick (<http://it.mathworks.com/matlabcentral/fileexchange/22992-lunar-azimuth-and-altitude-estimation-algorithm/>). The optical alignment of the PFR was frequently checked by fine scanning the lunar disk (with exception of the 2014 winter). The instrument was installed during almost every winter starting from February 2014, even with different time coverages. Data from a total of 16 lunar cycles were acquired, resulting in 56 measurement periods in the period 2014–2019 (day and/or night, Table 4).

Fig. 4 shows results from two measurements periods obtained at Ny-

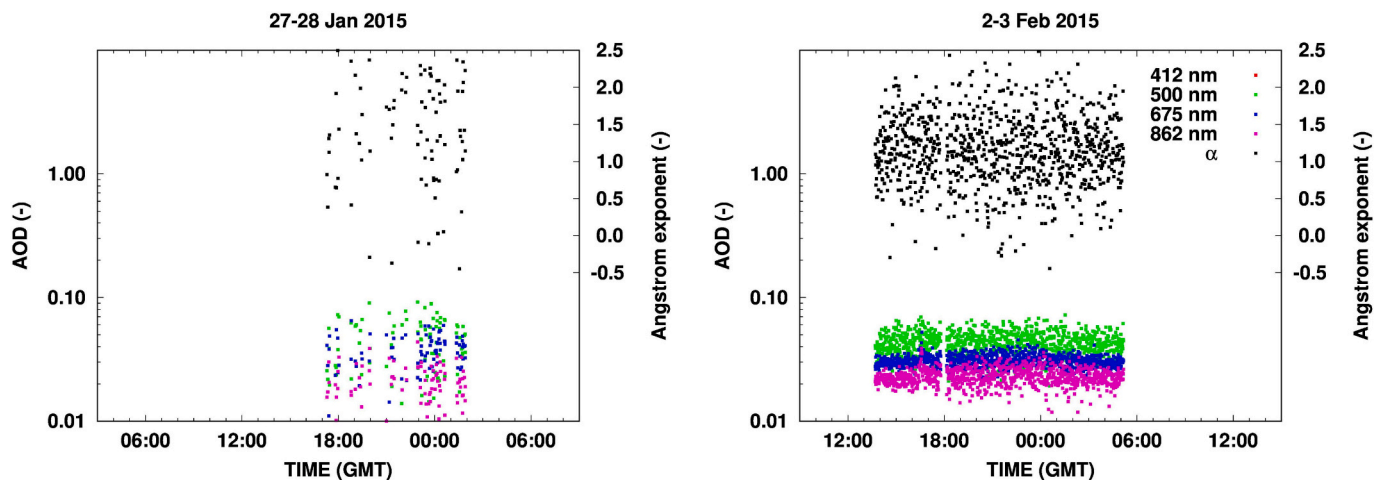


Fig. 4. Spectral AOD obtained using the PFR at Ny-Ålesund on January 27–28, 2015, with 50 % of lunar illumination (left), and on February 2–3, 2015, with 96 % illumination (right).

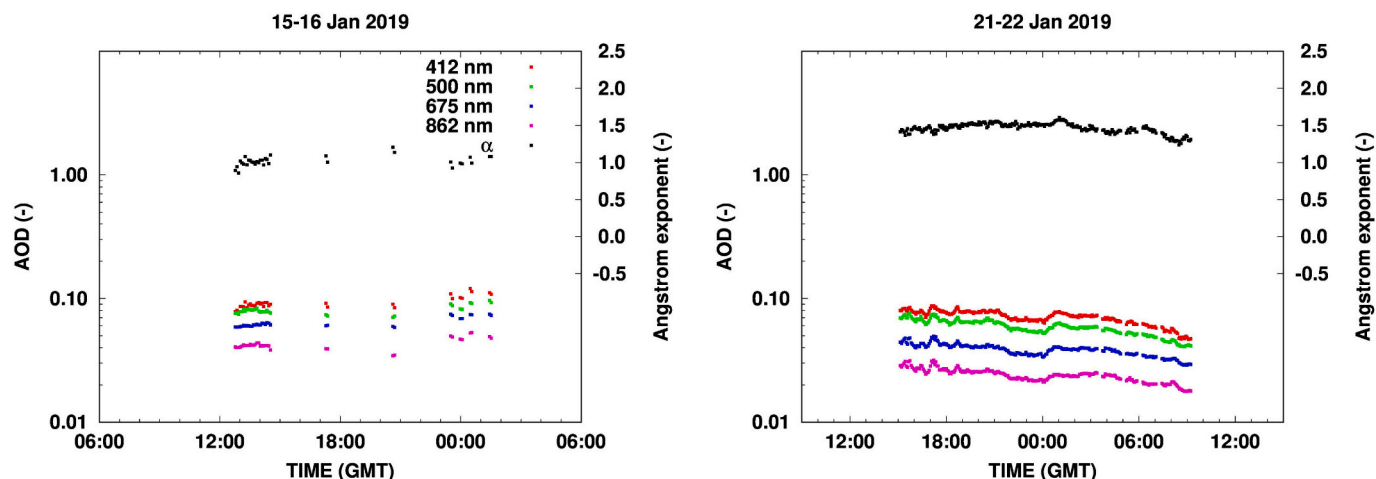


Fig. 5. Spectral AOD obtained using the PFR2015 at Ny-Ålesund on January 15–16, 2019, with 62 % of lunar illumination (left), and on January 21–22, 2019, with 100 % illumination (full Moon, right).

Ålesund with PFR for different Moon illumination values, similarly to Fig. 3. Again the noise on the AOD values is higher at low illumination and the spectral channels present different values: 39 % at 500 nm, 21 % at 675 nm, 31 % at 862 nm for the measurements of the night between 27 and 28 of January 2015 and 19 % at 500 nm, 10 % at 675 nm, 14 % at 862 nm for the measurements of the night between 2 and 3 of February 2015. For α the noise value passed from 50 % to 39 %.

Comparing these results with those obtained using the PFR2015, the improvement in the results obtained in terms of stability of AOD values is evident. Fig. 5 shows the measurements obtained with PFR2015 on January 15–16, 2019 (near first quarter) and on January 21–22, 2019 (full Moon). In this case the noise was evaluated to be 5 %, 3 %, 2 % and 4 % for the 4 wavelengths at low illumination and 3 %, 3 %, 3 % and 6 % at high illumination. For α the noise value passed from 4 % to 3 %.

Fig. B.8 shows hourly average values and associated standard deviations for the years 2014–2015. AOD values at 500 nm were mainly between 0.05 and 0.1, with few exceptions going up to 0.15. Even higher values must be attributed to thin clouds, since the corresponding α value collapses to values close to zero. Again, such values are comparable to the daily averages reported in Tomasi et al. (2012) for the beginning of the sun-photometry season, as well as with the star photometry data for years between 1997 and 2000. Similar results are reported by Toledano et al. (2012) and also by Sakerin et al. (2018) in Barentsburg, located about 100 Km southeast of Ny-Ålesund, during the years of observation.

Table 5

Comparison statistics for PFR vs. star photometer (hourly average values, for a total of 29 points) and for PFR vs. Cimel CE318-T (5 min average values, 64 points): average bias (PFR - star photometer or Cimel), root mean square difference (RMSD), standard deviation of the difference (SSD), expanded uncertainty (U95 = $\sqrt{Bias^2 + (2 \cdot SSD)^2}$) and Pearson correlation coefficient (PCC).

	Bias	RMSD	SSD	U95	PCC
<i>PFR vs. Star photometer</i>					
τ (412/420 nm)	–	–	–	–	–
τ (500 nm)	–0.003	0.007	0.006	0.013	0.48
τ (675 nm)	–0.007	0.009	0.006	0.013	0.43
τ (862 nm)	–0.002	0.005	0.004	0.009	0.41
α	0.2	0.4	0.3	0.6	0.43
<i>PFR vs. Cimel CE318-T</i>					
τ (412/440 nm)	–0.003	0.008	0.008	0.016	0.95
τ (500 nm)	0.007	0.009	0.005	0.013	0.97
τ (675 nm)	0.005	0.007	0.005	0.011	0.97
τ (862/870 nm)	0.009	0.010	0.005	0.013	0.96
α	–0.3	0.3	0.1	0.4	0.90

The measurements taken in Ny-Ålesund during January and February 2015 were also compared with AOD values retrieved by AWI using a star photometer. The star photometer has 17 spectral channels in the range between 420 and 1040 nm, including 500, 675, 862 nm. Fig. 8 shows the comparison of AOD at 500 nm and α in terms of hourly averages with standard deviation. The comparison of both AOD and α is acceptable, being within 0.02 for AOD and 0.5 for α . However, on January 27, 2015 α values were quite different between the two techniques. In Table 5 the statistics for this comparison for spectral AOD and for α are reported. Hourly averages were used, for a total of 29 data points. The table shows average bias, root mean square difference (RMSD), standard deviation of the difference (SSD), expanded uncertainty (U95) and Pearson correlation coefficient (PCC) for the difference between values of PFR and star photometer. These statistical parameters (bias, RMSD, SSD, U95) present values that are below the total uncertainty ones evaluated in Section 2.4 and reported in Table 3 for PFR (with the exception of U95 for α), confirming the validity and goodness of the measurements obtained in Ny-Ålesund. It is worth noting that this cannot be considered a real validation because the star data are prone to higher uncertainties and that horizontally inhomogeneous distribution of aerosol in the fjord could play a role when comparing measurements taken with the Moon and with stars, due to different positioning of the light source in the sky. This could partially justify the low PCC values reported in Table 5 for the PFR vs. star photometer comparison.

The installation of a sun-sky-lunar Cimel CE318-T in Ny-Ålesund in 2017 provided the opportunity for a comparative analysis to assess the accuracy of measurements obtained with the modified PFR2015. The lunar AOD data from the Cimel instrument were retrieved from the AERONET webpage, with a 5-min sampling rate. Unfortunately, the examination of the AOD time series between 2017 and 2020 revealed only a few instances of overlapping periods. In the first months of 2018, the Cimel instrument covered the entire polar night with a good frequency, whereas data for the PFR were only available to a limited extent. During this period, only January 30, 2018 witnessed concurrent measurements from both instruments, occurring between 3:00 am and 8:00 am. During the subsequent polar night, spanning from October 2018 to March 2019, the Cimel instrument covered October and February–March, while the PFR spanned from the end of November to the middle of February. This resulted in a singular overlapping period on February 18, 2019, from 5:00 pm to 10:00 pm. During the polar night of 2020, data collection was limited to measurements obtained solely from the PFR instrument. Unfortunately, no concurrent measurements from the Cimel instrument were available during this period.

Fig. 6 shows the 5-min averaged AOD comparison between the PFR and Cimel in Ny-Ålesund for the two measurement periods cited above.

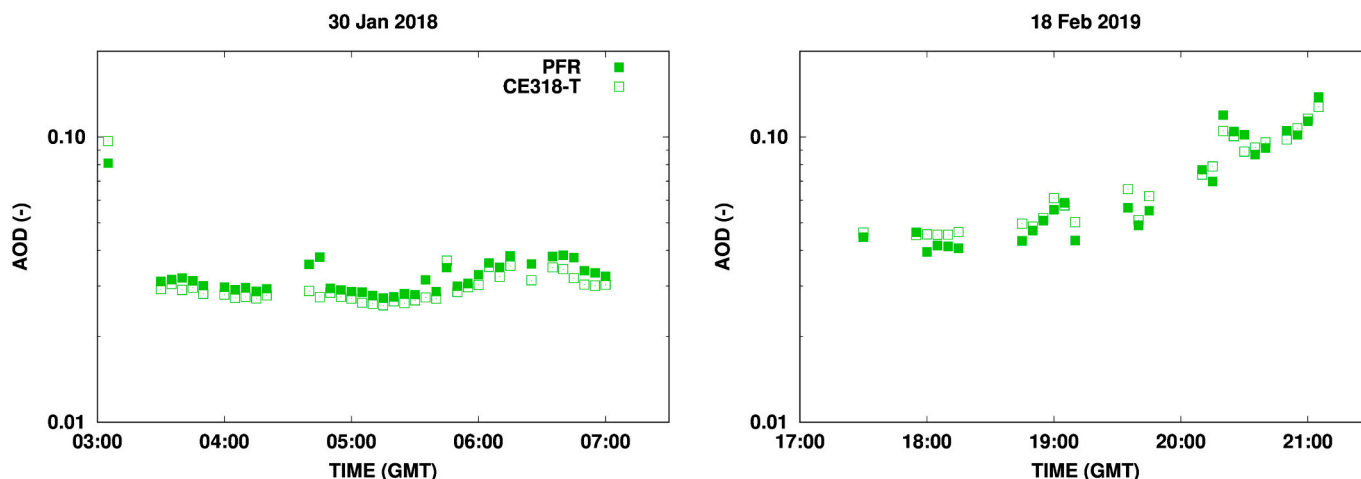


Fig. 6. Comparison of lunar AOD measurements between PFR and Cimel at Ny-Ålesund at the spectral channel 500 nm.

Based on these plots, it is evident that on January 30, 2018, both instruments consistently recorded stable behavior with AOD levels hovering around 0.04. There were minor variations between the readings of the two instruments. Conversely, on February 18, 2019, despite an increase in AOD values from 0.06 to 0.15, the measurements from both instruments continued to exhibit good agreement, effectively capturing the emerging trend. As for the PFR vs. star photometer comparison, 5 reports detailed statistics for the differences between the results obtained by the two instruments, using all data from the two valid periods, for AOD at the four wavelengths and for α . 5 min averages were used for the comparison, for a total of 64 data points. It is evident that bias, RMSD and SSD values are well below the corresponding uncertainty values evaluated in Table 3 for all spectral channels of PFR. Even the U95 parameter show low or comparable values to those of Table 3. Similar considerations applies to α values, considering the uncertainties reported at the end of Section 2.4. The Pearson correlation coefficient values resulted consistently high ($> = 0.95$ for AOD and $= 0.90$ for α) even considering that some wavelengths slightly differ between the two instruments, i.e., 412 and 862 nm for PFR and 440 and 870 nm for Cimel.

This analysis, although conducted over only few hours of measurement, highlights that Cimel and PFR give consistent results.

4. Conclusions and recommendations

Two commercial sun photometers have been modified to be able to detect the very weak spectral lunar irradiance coming from the Moon during the period from first to third quarter of the Moon phase. They have been used at two stations in the Arctic during different periods, spanning the years from 2012 to 2019. Using the *exo*-atmospheric model ROLO for the evaluation of the radiation reflected by the Moon, we evaluated the AOD at the 4 wavelengths of the two instruments, together with their uncertainties. Uncertainties of the moon photometer were found to be only slightly higher than those obtainable with sun photometry, being in the range 0.006–0.030 for all channels of the two instruments.

As expected the AOD values are noisier at low Moon illumination, while more stable moving towards full Moon.

The AOD and α values evaluated at the two sites are in accordance with those reported in the literature for the periods of the year nearby the polar night when sun photometry is possible (e.g. October/March).

The comparison with star photometry data in Ny-Ålesund confirmed the reliability of the AOD values derived from lunar observations. More, the presence since 2017 of a commercial Cimel CE318-T allowed a direct comparison of the results, giving average differences of 0.006 at maximum, therefore lower than the evaluated uncertainties.

In this work we demonstrated that lunar photometry is a suitable measurement technique also in polar regions, where AOD is very low and sunlight is not present for a long period during the year.

The results presented in this paper are the first, to our knowledge, that provide time series of the magnitude and variation of AOD during the dark months of winter at high northern latitudes. Spanning nearly 10 degrees of latitude and distant from one another, Barrow and Ny-Ålesund are considered to be representative of two regions of the Arctic, sources and pathways of aerosol transported into the Arctic differ between the Pacific and the Atlantic sectors, thus their AOD climatologies differ somewhat (Stone et al., 2014b). Although limited, the data so far collected are valuable for a myriad of studies. These include filling gaps in existing AOD climatologies, validation of independently derived AOD using remote sensing techniques, verifying climate model simulations. In conjunction with radiometric measurements of the surface radiation budget, nighttime radiative forcing by aerosols and thin clouds can be quantified. In conjunction with Lidar studies the interaction between aerosols and clouds can also be evaluated.

CRediT authorship contribution statement

Mauro Mazzola: Writing – review & editing, Writing – original draft, Visualization, Software, Methodology, Investigation, Formal analysis, Data curation, Conceptualization. **Robert S. Stone:** Writing – review & editing, Methodology, Data curation, Conceptualization. **Natalia Kouremeti:** Writing – review & editing, Methodology, Investigation, Formal analysis, Data curation, Conceptualization. **Vito Vitale:** Writing – review & editing, Supervision, Conceptualization. **Julian Gröbner:** Writing – review & editing, Methodology, Investigation, Conceptualization. **Kerstin Stebel:** Writing – review & editing, Investigation, Data curation. **Georg H. Hansen:** Writing – review & editing, Investigation, Data curation. **Thomas C. Stone:** Writing – review & editing, Software, Investigation, Data curation. **Christoph Ritter:** Writing – review & editing, Investigation, Data curation. **Simone Pulimeno:** Writing – review & editing, Writing – original draft, Visualization, Methodology, Investigation, Data curation.

Declaration of competing interest

The authors declare that they have no known competing financial interests or personal relationships that could have appeared to influence the work reported in this paper.

Data availability

Data will be made available on request.

Acknowledgements

The University of Colorado supported the development of the SP02 lunar photometer. Special thanks goes to J. Wendell and D. Longenecker for design and initial data processing. A. Jordan and E. Hall modified the Eppley solar tracker. E. Dutton provided project guidance and we thank the BRW field technicians, who deployed and monitored the system

through a harsh Arctic winter. Authors would like to thank C. Wehrli for his efforts in the development of the Lunar-PFR and the Norwegian Polar Institute personnel for their continuous support of the joint PMOD/WRC and NILU aerosol optical depth measurements in Ny-Ålesund. Authors would like also to thank Victoria E. Cachorro Revilla and Christoph Ritter for their effort in establishing and maintaining Ny_Alesund_AWI AERONET site.

Appendix A. List of acronyms, symbols and units

A.1. Acronyms

AERONET	Aerosol Robotic Network
AOD	Aerosol Optical Depth
CALIOP	Cloud-Aerosol Lidar with Orthogonal Polarisation
EAI	Exo-Atmospheric Irradiance
MFRSR	MultiFilter Rotating Shadowband Radiometer
NASA	National Aeronautics and Space Administration
NOAA	National Oceanic and Atmospheric Administration
PFR	Precision Filter Radiometer, by PMOD/WRC
PID	Proportional-Integral-Derivative
PMOD/WRC	Physical Meteorological Observatory in Davos / World Radiation Centre
RIMO	ROLO Implementation for Moon-photometry Observation
RMSD	Root Mean Square Difference
ROLO	RObotic Lunar Observatory
SP02	Sun-Photometer 02, by Carter Scott
SSD	Standard Deviation of Differences
U95	Expanded uncertainty

A.2. Symbols

α	Angström exponent
A_λ	spectral lunar albedo at wavelength λ
d	ratio between the actual Moon-observer distance and the mean radius of the Moon's orbit around the Earth (384,400 km)
E_λ	spectral standard extraterrestrial solar irradiance
$J_\lambda, J_{0,\lambda}$	spectral signal measured at wavelength λ and corresponding calibration factor
$J_\lambda^*, J_{0,\lambda}^*$	normalized spectral signal at wavelength λ and corresponding calibration factor
λ	wavelength of the considered radiation
m	optical relative air mass
Ω	solid angle of the Moon
r, r_0	Earth-Sun distance and its mean value, equal to 1 AU
R	ratio between the actual Earth-Sun distance r and r_0 , hence numerically equivalent to the Sun-Earth distance expressed in astronomical units (AU)
τ_λ	spectral aerosol optical depth at wavelength λ

A.3. Units

AU	Astronomical Units
DU	Dobson Units

Appendix B. Hourly values for all measurement periods

In the following figures the hourly averages and standard deviations of AOD at 500 nm and Angström Exponent will be shown: Fig. B.7 for Barrow and Figs. B.8, B.9, B.10 for Ny-Ålesund.

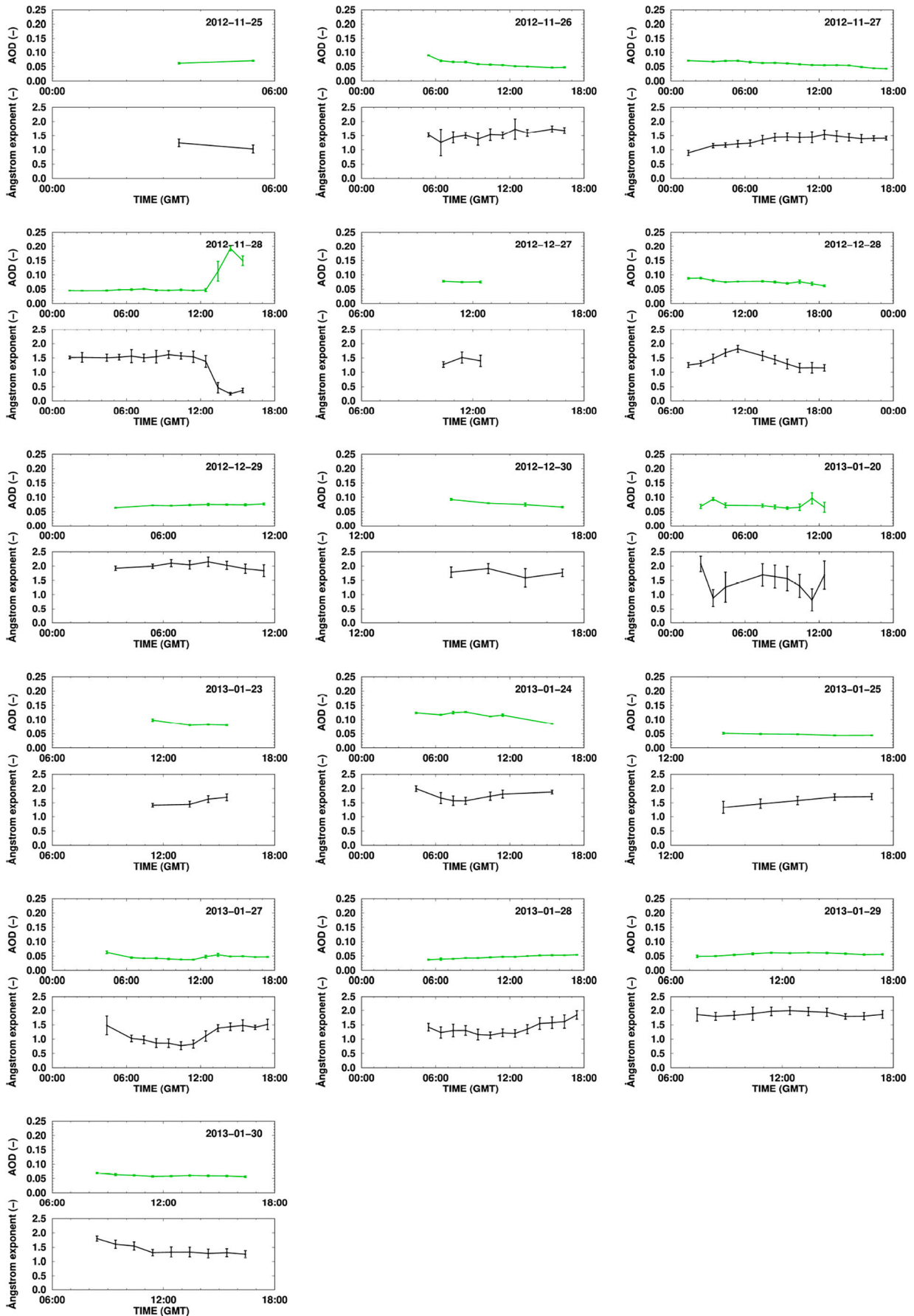


Fig. B.7. Hourly averages and standard deviations of AOD at 500 nm and Angström Exponent values obtained during 16 measuring periods at Barrow.

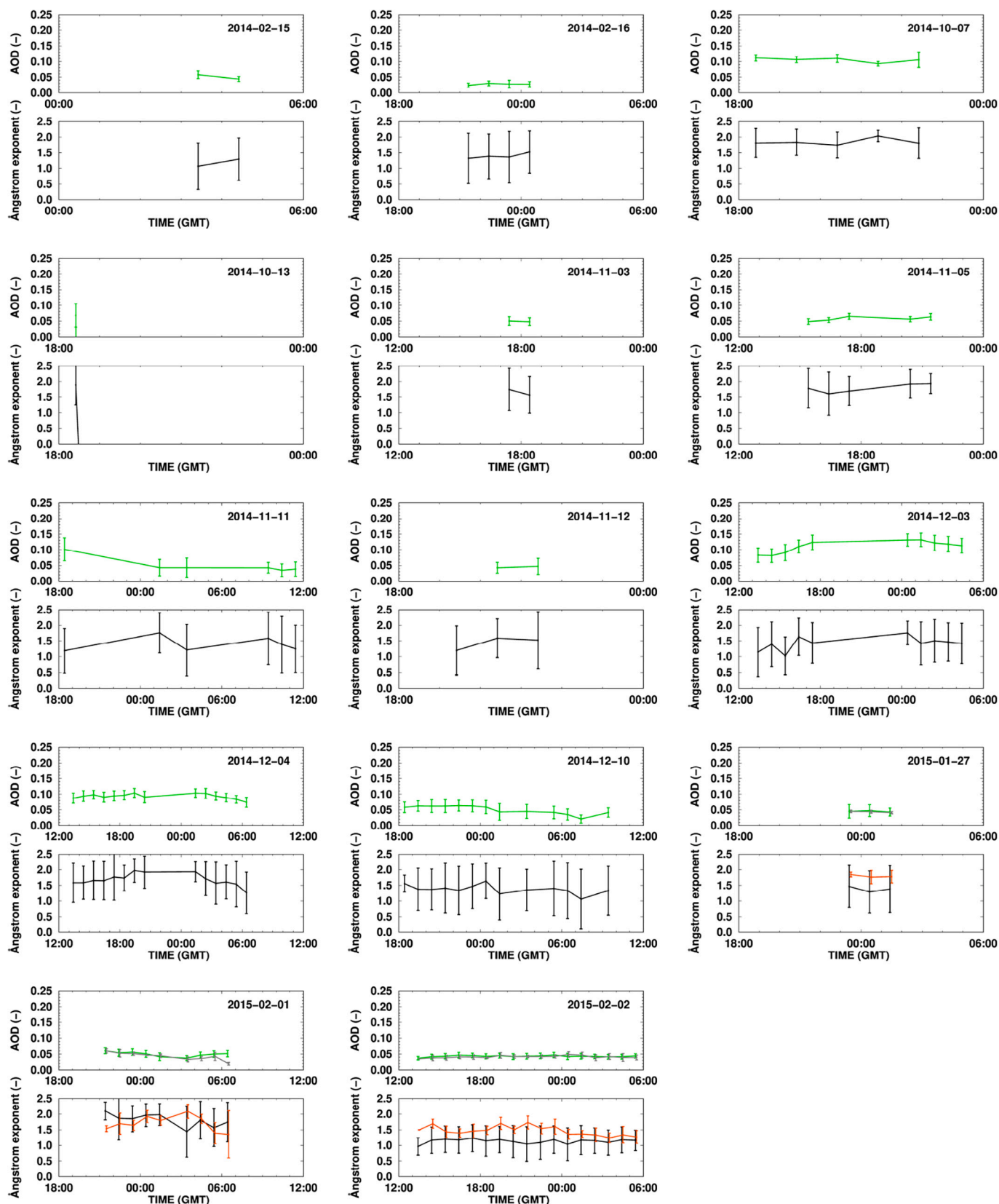


Fig. B.8. Hourly averages and standard deviations of AOD at 500 nm and Angström Exponent values obtained during 17 measuring periods between 2014 and 2015 at Ny-Ålesund. The grey values for AOD and the orange values for α where measured by the star photometer operated by AWI.

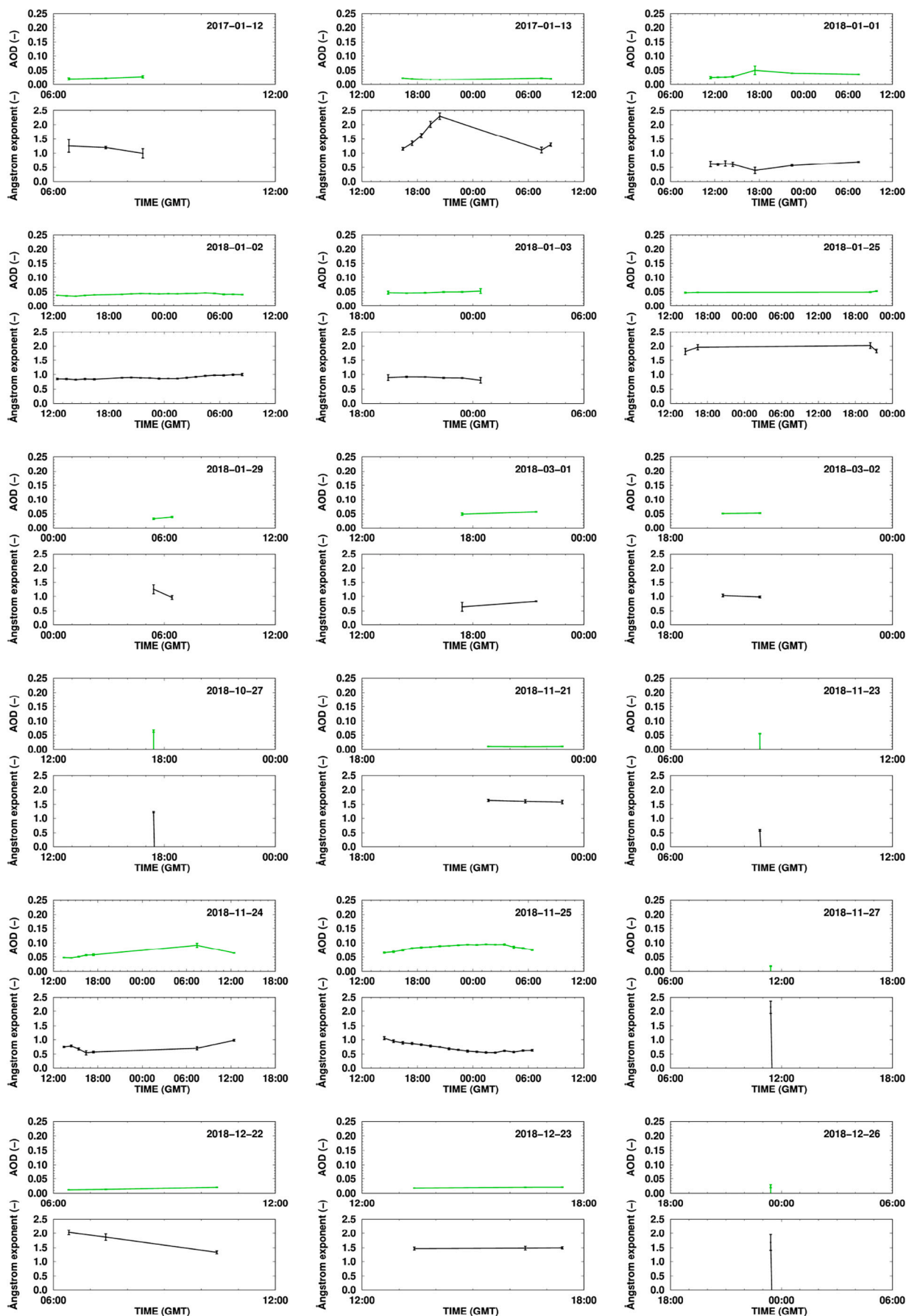


Fig. B.9. Same as in Fig. B.8 but for year 2017 and 2018.

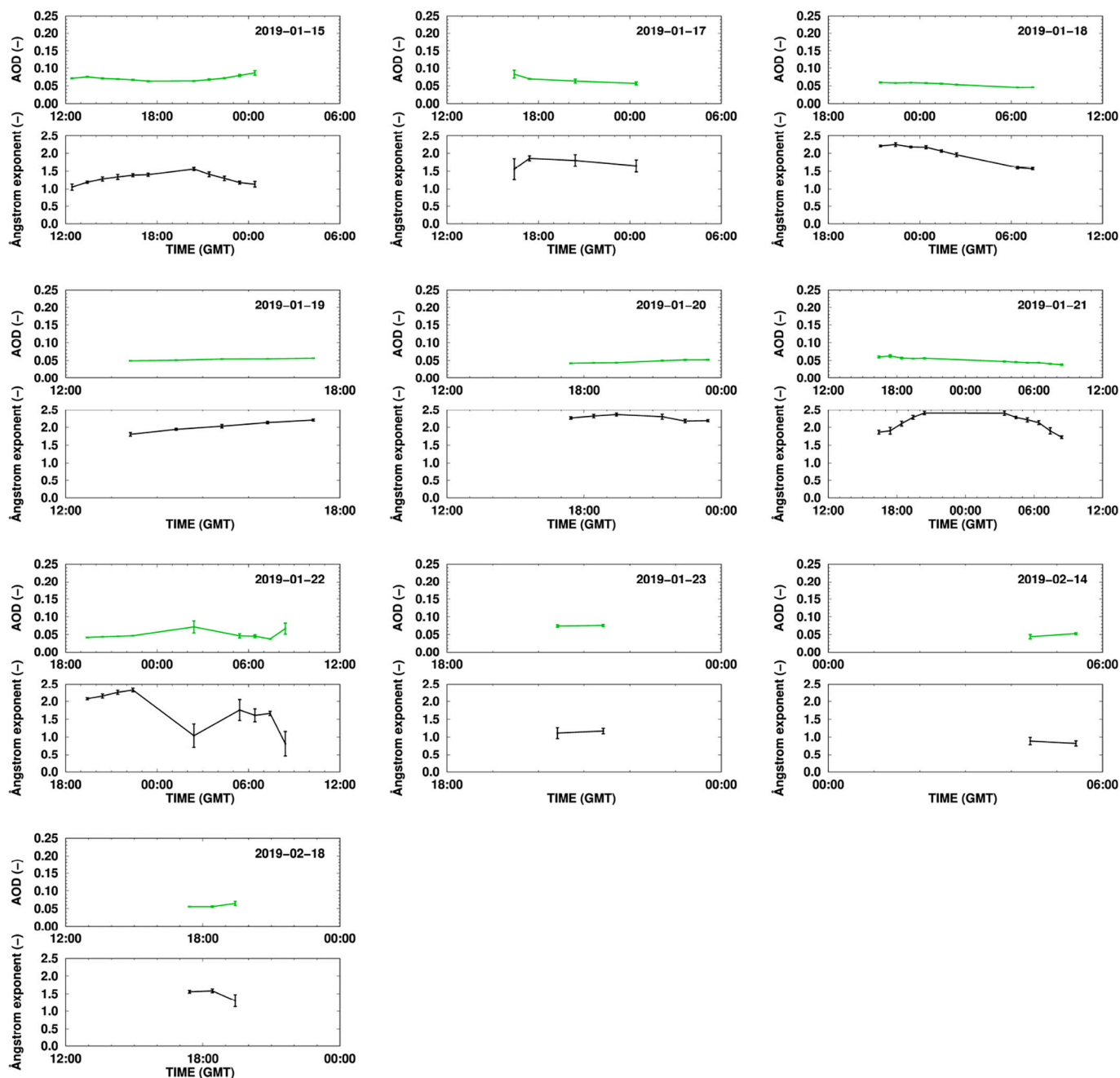


Fig. B.10. Same as in Fig. B.8 but for year 2019.

References

Ångström, A., 1929. On the atmospheric transmission of sun radiation and on dust in the air. *Geogr. Ann.* 11, 156–166. <https://doi.org/10.1080/20014422.1929.11880498>.

Barreto, A., Cuevas, E., Damiri, B., Guirado, C., Berkoff, T., Berjón, A.J., Hernández, Y., Almansa, F., Gil, M., 2013a. A new method for nocturnal aerosol measurements with a lunar photometer prototype. *Atmos. Meas. Tech.* 6, 585–598. URL: <https://amt.copernicus.org/articles/6/585/2013/> <https://doi.org/10.5194/amt-6-585-2013>. publisher: Copernicus GmbH.

Barreto, A., Cuevas, E., Damiri, B., Romero, P.M., Almansa, F., 2013b. Column water vapor determination in night period with a lunar photometer prototype. *Atmos. Meas. Tech.* 6, 2159–2167. URL: <https://amt.copernicus.org/articles/6/2159/2013/> <https://doi.org/10.5194/amt-6-2159-2013>. publisher: Copernicus GmbH.

Barreto, A., Cuevas, E., Granados-Muñoz, M.J., Alados-Arboledas, L., Romero, P.M., Gröbner, J., Kouremeti, N., Almansa, A.F., Stone, T., Toledano, C., Román, R., Sorokin, M., Holben, B., Canini, M., Yela, M., 2016. The new sun-sky-lunar Cimel

CE318-T multiband photometer – a comprehensive performance evaluation. *Atmos. Meas. Tech.* 9, 631–654. URL: <https://amt.copernicus.org/articles/9/631/2016/amt-9-631-2016-discussion.html> <https://doi.org/10.5194/amt-9-631-2016>. publisher: Copernicus GmbH.

Barreto, A., Román, R., Cuevas, E., Berjón, A.J., Almansa, A.F., Toledano, C., González, R., Hernández, Y., Blarel, L., Goloub, P., Guirado, C., Yela, M., 2017. Assessment of nocturnal aerosol optical depth from lunar photometry at the Izaña high mountain observatory. *Atmos. Meas. Tech.* 10, 3007–3019. URL: <https://amt.copernicus.org/articles/10/3007/2017/> <https://doi.org/10.5194/amt-10-3007-2017>.

Barreto, A., Román, R., Cuevas, E., Pérez-Ramírez, D., Berjón, A.J., Kouremeti, N., Kazadzis, S., Gröbner, J., Mazzola, M., Toledano, C., Benavent-Oltra, J.A., Doppler, L., Juryšek, J., Almansa, A.F., Victori, S., Maupin, F., Guirado-Fuentes, C., González, R., Vitale, V., Goloub, P., Blarel, L., Alados-Arboledas, L., Woolliams, E., Taylor, S., Antuna, J.C., Yela, M., 2019. Evaluation of night-time aerosols measurements and lunar irradiance models in the frame of the first multi-instrument nocturnal intercomparison campaign. *Atmos. Environ.* 202, 190–211. URL:

- <https://www.sciencedirect.com/science/article/pii/S1352231019300287> <https://doi.org/10.1016/j.atmosenv.2019.01.006>.
- Berkoff, T.A., Sorokin, M., Stone, T., Eck, T.F., Hoff, R., Welton, E., Holben, B., 2011. Nocturnal aerosol optical depth measurements with a small-aperture automated photometer using the moon as a light source. *J. Atmos. Ocean. Technol.* 28, 1297–1306. <https://doi.org/10.1175/JTECH-D-10-05036.1>.
- Brunamonti, S., Martucci, G., Romanens, G., Poltera, Y., Wienhold, F.G., Hervo, M., Haefele, A., Navas-Guzmán, F., 2021. Validation of aerosol backscatter profiles from raman lidar and ceilometer using balloon-borne measurements. *Atmos. Chem. Phys.* 21, 2267–2285. URL: <https://acp.copernicus.org/articles/21/2267/2021/> <https://doi.org/10.5194/acp-21-2267-2021>.
- Esposito, F., Serio, C., Pavese, G., Auriemma, G., Satriano, C., 1998. Measurements of nighttime atmospheric optical depth preliminary data from a mountain site in southern Italy. *J. Aerosol Sci.* 29, 1213–1218. URL: <https://www.sciencedirect.com/science/article/pii/S0021850298000111> [https://doi.org/10.1016/S0021-8502\(98\)00011-1](https://doi.org/10.1016/S0021-8502(98)00011-1).
- Esposito, F., Mari, S., Pavese, G., Serio, C., 2003. Diurnal and Nocturnal Measurements of Aerosol Optical Depth at a Desert Site in Namibia. *Aerosol Sci. Technol.* 37, 392–400. <https://doi.org/10.1080/027868203009972>.
- Forgan, B., 2005. Aerosol optical depth monitoring as part of the solar and terrestrial radiation network australian bureau of meteorology. In: Barrie, L.A., Wehrli, C. (Eds.), WMO/GAW Experts Workshop on a Global Surface-Based Network for Long Term Observations of Column Aerosol Optical Properties (8–10 March 2004), WMO. World Meteorological Organization Global Atmosphere Watch, Geneva, Switzerland, pp. 43–48. URL: <https://library.wmo.int/idurl/4/41246>.
- Harrison, L., Michalsky, J., 1994. Objective algorithms for the retrieval of optical depths from ground-based measurements. *Appl. Opt.* 33, 5126–5132. <https://doi.org/10.1364/AO.33.005126>.
- Herber, A., Thomason, L.W., Gernandt, H., Leiterer, U., Nagel, D., Schulz, K.H., Kaptur, J., Albrecht, T., Notholt, J., 2002. Continuous day and night aerosol optical depth observations in the Arctic between 1991 and 1999. *J. Geophys. Res. Atmos.* 107. <https://doi.org/10.1029/2001JD000536>.
- Herrero del Barrio, C., Mateos, D., Román, R., González, R., Herrero-Anta, S., González-Fernández, D., Calle, A., Toledano, C., Cachorro, V.E., De Frutos Baraja, A.M., 2023. Analysis of daytime and night-time aerosol optical depth from solar and lunar photometry in Valladolid (Spain). *Remote Sens.* 15. <https://doi.org/10.3390/rs15225362>. URL: <https://www.mdpi.com/2072-4292/15/22/5362>.
- Hoffmann, A., Ritter, C., Stock, M., Maturilli, M., Eckhardt, S., Herber, A., Neuber, R., 2010. Lidar measurements of the Kasatochi aerosol plume in August and September 2008 in Ny-Ålesund, Spitsbergen. *J. Geophys. Res. Atmos.* 115. <https://doi.org/10.1029/2009JD013039>. URL: <https://onlinelibrary.wiley.com/doi/abs/10.1029/2009JD013039>.
- IPCC, 2023. Summary for Policymakers. In: *Climate Change 2023: Synthesis Report. Contribution of Working Groups I, II and III to the Sixth Assessment Report of the Intergovernmental Panel on Climate Change* (Core Writing Team. IPCC, Geneva, Switzerland, pp. 1–34. <https://doi.org/10.59327/IPCC/AR6-9789291691647.001>.
- Kaufman, Y.J., Joseph, J.H., 1982. Determination of surface albedos and aerosol extinction characteristics from satellite imagery. *J. Geophys. Res. Oceans* 87, 1287–1299. <https://doi.org/10.1029/JC087iC02p01287>. URL: <https://agupubs.onlinelibrary.wiley.com/doi/abs/10.1029/JC087iC02p01287>.
- Kieffer, H.H., Stone, T.C., 2005. The Spectral Irradiance of the Moon. *Astron. J.* 129, 2887. <https://doi.org/10.1086/430185>. URL: <https://iopscience.iop.org/article/10.1086/430185/meta>.
- Lubin, D., Vogelmann, A.M., 2006. A climatologically significant aerosol longwave indirect effect in the Arctic. *Nature* 439, 453–456. <https://doi.org/10.1038/nature04449> number: 7075 Publisher: nature Publishing Group. URL: <https://www.nature.com/articles/nature04449>.
- Mazzola, M., Lanconelli, C., Lupi, A., Busetto, M., Vitale, V., Tomasi, C., 2010. Columnar aerosol optical properties in the Po Valley, Italy, from MFRSR data. *J. Geophys. Res. Atmos.* 115. <https://doi.org/10.1029/2009JD013310>. URL: <https://onlinelibrary.wiley.com/doi/abs/10.1029/2009JD013310>.
- Mazzola, M., Stone, R., Herber, A., Tomasi, C., Lupi, A., Vitale, V., Lanconelli, C., Toledano, C., Cachorro, V., O'Neill, N., Shiobara, M., Aaltonen, V., Stebel, K., Zielinski, T., Petelski, T., Ortiz de Galisteo, J., Torres, B., Berjon, A., Goloub, P., Li, Z., Blarel, L., Abboud, I., Cuevas, E., Stock, M., Schulz, K.H., Virkkula, A., 2012. Evaluation of sun photometer capabilities for retrievals of aerosol optical depth at high latitudes: the POLAR-AOD intercomparison campaigns. *Atmos. Environ.* 52, 4–17. <https://doi.org/10.1016/j.atmosenv.2011.07.042>. URL: <https://www.sciencedirect.com/science/article/pii/S1352231011007862>.
- Pérez-Ramírez, D., Aceituno, J., Ruiz, B., Olmo, F.J., Alados-Arboledas, L., 2008. Development and calibration of a star photometer to measure the aerosol optical depth: Smoke observations at a high mountain site. *Atmos. Environ.* 42, 2733–2738. <https://doi.org/10.1016/j.atmosenv.2007.06.009>. URL: <https://www.sciencedirect.com/science/article/pii/S1352231007005699>.
- Perrone, M.R., Lorusso, A., Romano, S., 2022. Diurnal and nocturnal aerosol properties by aeronet sun-sky-lunar photometer measurements along four years. *Atmos. Res.* 265, 105889. <https://doi.org/10.1016/j.atmosres.2021.105889>. URL: <https://www.sciencedirect.com/science/article/pii/S0169809521004452>.
- Román, R., González, R., Toledano, C., Barreto, A., Pérez-Ramírez, D., Benavent-Oltra, J. A., Olmo, F.J., Cachorro, V.E., Alados-Arboledas, L., de Frutos, A.M., 2020. Correction of a lunar-irradiance model for aerosol optical depth retrieval and comparison with a star photometer. *Atmospheric. Meas. Tech.* 13, 6293–6310. <https://doi.org/10.5194/amt-13-6293-2020>. URL: <https://amt.copernicus.org/articles/13/6293/2020/>.
- Sakerin, S.M., Kabanov, D.M., Radionov, V.F., Chernov, D.G., Turchinovich, Y.S., Lubo-Lesnichenko, K.E., Prakhov, A.N., 2018. Generalization of results of atmospheric aerosol optical depth measurements on spitsbergen archipelago in 2011–2016. *Atmos. Ocean Opt.* 31, 163–170. <https://doi.org/10.1134/S1024856018020112>.
- Schuster, G.L., Dubovik, O., Holben, B.N., 2006. Angstrom exponent and bimodal aerosol size distributions. *J. Geophys. Res. Atmos.* 111. <https://doi.org/10.1029/2005JD006328>. URL: <https://agupubs.onlinelibrary.wiley.com/doi/abs/10.1029/2005JD006328>.
- Shaw, G.E., 1983. Sun photometry. *Bull. Am. Meteorol. Soc.* 64, 4–10. URL: <http://www.jstor.org/stable/26223258>.
- Shaw, G.E., Reagan, J.A., Herman, B.M., 1973. Investigations of atmospheric extinction using direct solar radiation measurements made with a multiple wavelength radiometer. *J. Appl. Meteorol. Climatol.* 12, 374–380. [https://doi.org/10.1175/1520-0450\(1973\)012<0374:IOAEUD>2.0.CO;2](https://doi.org/10.1175/1520-0450(1973)012<0374:IOAEUD>2.0.CO;2). URL: https://journals.ametsoc.org/view/journals/apme/12/2/1520-0450_1973_012_0374_ioaeud_2_0_co_2.xml.
- Stone, R., Berkoff, T., Stone, T., Wendell, J., Longenecker, D., 2014a. Monitoring aerosol optical depth during the arctic night: Development of a lunar photometer for use at the noaa barrow observatory. In: *Proceedings of the NOAA ESRL Global Monitoring Annual Conference 2014*. NOAA ESRL Global Monitoring Division pp. P-39.
- Stone, R., Sharma, S., Herber, A., Eleftheriadis, K., Nelson, D., 2014b. A characterization of Arctic aerosols on the basis of aerosol optical depth and black carbon measurements. *Elementa* 2. <https://doi.org/10.12952/journal.elementa.000027>.
- Toledano, C., Cachorro, V.E., Berjon, A., de Frutos, A.M., Sorribas, M., de la Morena, B. A., Goloub, P., 2007. Aerosol optical depth and Ångström exponent climatology at el arenosillo aeronet site (Huelva, Spain). *Q. J. R. Meteorol. Soc.* 133, 795–807. <https://doi.org/10.1002/qj.54>. URL: <https://rmets.onlinelibrary.wiley.com/doi/abs/10.1002/qj.54>.
- Toledano, C., Cachorro, V., Gausa, M., Stebel, K., Aaltonen, V., Berjón, A., Ortiz de Galisteo, J., de Frutos, A., Bennouna, Y., Blindheim, S., Myhre, C., Zibordi, G., Wehrli, C., Kratzer, S., Hakansson, B., Carlund, T., de Leeuw, G., Herber, A., Torres, B., 2012. Overview of sun photometer measurements of aerosol properties in Scandinavia and Svalbard. *Atmos. Environ.* 52, 18–28. <https://doi.org/10.1016/j.atmosenv.2011.10.022> physical, chemical, optical and radiative properties of polar aerosols – IPY 2007 – 2008. URL: <https://www.sciencedirect.com/science/article/pii/S1352231011010818>.
- Tomasi, C., Lupi, A., Mazzola, M., Stone, R.S., Dutton, E.G., Herber, A., Radionov, V.F., Holben, B.N., Sorokin, M.G., Sakerin, S.M., Terpigova, S.A., Sobolewski, P.S., Lanconelli, C., Petkov, B.H., Busetto, M., Vitale, V., 2012. An update on polar aerosol optical properties using POLAR-AOD and other measurements performed during the International Polar Year. *Atmos. Environ.* 52, 29–47. <https://doi.org/10.1016/j.atmosenv.2012.02.055>. URL: <https://www.sciencedirect.com/science/article/pii/S1352231012001707>.
- Uchiyama, A., Shiobara, M., Kobayashi, H., Matsunaga, T., Yamazaki, A., Inei, K., Kawai, K., Watanabe, Y., 2019. Nocturnal aerosol optical depth measurements with modified sky radiometer POM-02 using the moon as a light source. *Atmos. Meas. Tech.* 12, 6465–6488. <https://doi.org/10.5194/amt-12-6465-2019> publisher: Copernicus GmbH. URL: <https://amt.copernicus.org/articles/12/6465/2019/>.
- Wehrli, C., 2005. Gawpfr: A network of aerosol optical depth observations with precision filter radiometers. In: Barrie, L.A., Wehrli, C. (Eds.), WMO/GAW Experts Workshop on a Global Surface-Based Network for Long Term Observations of Column Aerosol Optical Properties (8–10 March 2004), WMO. World Meteorological Organization Global Atmosphere Watch, Geneva, Switzerland, pp. 36–39. URL: <https://library.wmo.int/idurl/4/41246>.
- Zhao, X., Huang, K., Fu, J.S., Abdullaev, S.F., 2022. Long-range transport of asian dust to the arctic: identification of transport pathways, evolution of aerosol optical properties, and impact assessment on surface albedo changes. *Atmos. Chem. Phys.* 22, 10389–10407. <https://doi.org/10.5194/acp-22-10389-2022>. URL: <https://acp.copernicus.org/articles/22/10389/2022/>.
- Zhou, M., Wang, J., Chen, X., Xu, X., Colarco, P.R., Miller, S.D., Reid, J.S., Kondragunta, S., Giles, D.M., Holben, B., 2021. Nighttime smoke aerosol optical depth over u.s. rural areas: first retrieval from VIIRS moonlight observations. *Remote Sens. Environ.* 267, 112717. <https://doi.org/10.1016/j.rse.2021.112717>. URL: <https://www.sciencedirect.com/science/article/pii/S00344257211004375>.